Utilizing pre-polarization to enhance SNMR signals—effect of imperfect switch-off

Thomas Hiller [ID], Raphael Dlugosch and Mike Müller-Petke

Leibniz Institute for Applied Geophysics, Stilleweg 2, 30652 *Hannover, Germany. E-mail: Thomas.Hiller@leibniz-liag.de*

SUMMARY
Surface nuclear magnetic resonance (SNMR) is a well-established technique for the hydroge-ological characterization of the subsurface up to depths of about 150 m. Recently, SNMR has been adapted to investigate also the shallow unsaturated zone with small surface loop setups. Due to the decreased volume, a pre-polarization (PP) field prior to the classical spin excitation is applied to enhance the measured response signal. Depending on the strength and orientation of the applied PP-field, the enhancement can often reach several orders of magnitude in the vicinity of the PP-loop. The theoretically achievable enhancement depends on the assumption of an adiabatic, that is perfect, switch-off of the corresponding PP-field. To study the effect of imperfect switch-off, we incorporate full spin dynamics simulations into the SNMR forward modelling. The affected subsurface volume strongly depends on the chosen PP switch-off ramp and the geometry of the loop setup. Due to the imperfect switch-off, the resulting SNMR sounding curves can have significantly decreased signal amplitudes. For comparison, the sig-nal amplitudes of either a 1 ms exponential or linear switch-off ramp are reduced by 17 and 65 per cent, respectively. Disregarding this effect would therefore yield an underestimation of the corresponding subsurface water content of similar magnitude.

Key words: Hydrogeophysics; Electromagnetic theory; Numerical modelling.

1 INTRODUCTION

Surface nuclear magnetic resonance (SNMR), the surface-based variant of nuclear magnetic resonance (NMR), is one of the 'younger' methods used in applied hydrogeophysics. It has evolved over the last three decades to a reliable and well-established method to characterize near surface aquifer systems (e.g. Legchenko *et al.* 2004; Vouillamoz *et al.* 2011; Behroozmand *et al.* 2015). SNMR is the only non-destructive surface method that allows a direct depth-resolved quantification of the water content of such aquifer systems. Furthermore, the measured signal also carries information about the corresponding pore space and therefore can be used to establish relationships between the porous medium and its hydraulic prop-erties (e.g. Seevers 1966; Mohnke & Yaramanci 2008; Dlugosch *et al.* 2013). Over the years, SNMR underwent several iterations of improvement in terms of hardware development, signal process-ing and forward/inverse modelling. It is successfully in use as a magnetic resonance tomography (MRT) tool to investigate 2-D and 3-D subsurface structures (e.g. Hertrich *et al.* 2007; Hertrich 2008; Legchenko *et al.* 2011; Dlugosch *et al.* 2014; Jiang *et al.* 2016, 2018). By now, it is also commonly applied together with other geo-physical techniques like vertical electrical sounding (VES), electri-cal resistivity tomography (ERT) or ground penetrating radar (GPR) to increase structural model resolution and reduce the ambiguity of

a single method (e.g. Vouillamoz *et al.* 2007; Günther & Müller-Petke 2012; Costabel *et al.* 2017; Jiang *et al.* 2017; Skibbe *et al.* 2018).

Because of the weak NMR signal strengths involved, SNMR is generally prone to electromagnetic noise. When targeting the shal-low unsaturated zone with small loop layouts, the noise sensitivity is even more troublesome due to the even weaker NMR signals. To handle electromagnetic noise, several efficient noise cancella-tion techniques have been developed (e.g. Costabel & Müller-Petke 2014; Larsen *et al.* 2014; Müller-Petke & Costabel 2014). A com-prehensive overview on SNMR post-processing techniques can be found in Müller-Petke *et al.* (2016). Besides the use of noise cancel-lation techniques, there are other approaches available to increase the signal-to-noise ratio (SNR) of SNMR measurements. One is the application of adiabatic fast passage pulses (AP), where the ampli-tude and frequency of the excitation pulse is modulated in a time short compared to the relaxation times (e.g. Powles 1958; Tannùs & Garwood 1997; Grunewald *et al.* 2016; Grombacher 2018). The term *adiabatic* describes the rotational motion of the magnetiza-tion vector in relation to the varying magnetic field. The closer the magnetization is 'locked' to the magnetic field the more adiabatic is the process. In the presence of inhomogeneous excitation fields (general case when using surface loops), this yields a spatially more homogeneous excitation and therefore enhanced signal amplitudes

compared to the standard on-resonance (OR) excitation which operates at the resonance frequency. AP-excitation has its origins in other fields of NMR and is applied in medical imaging and microscopy (e.g. Uğurbil *et al.* 1988; van Zijl *et al.* 1996). However, until today OR-excitation is by far the most common excitation technique used in SNMR, whereas AP-excitation has been introduced to SNMR just within the past few years (Grunewald *et al.* 2016).

Another technique to increase the SNR of SNMR measurements is the pre-polarization (PP) of the net magnetization by applying an enhanced background static magnetic field prior to performing the actual measurement at a weaker field (Packard & Varian 1954). Therefore, it is also possible to conduct NMR measurements in the weak Earth's magnetic field if a proper pre-polarization is applied (e.g. Melton & Pollak 1971; Planinšič *et al.* 1994; Callaghan *et al.* 1997). The effect of pre-polarization to SNMR measurements (SNMR-PP) with small loop setups ($d_{pp} \approx 5$ m) was conceptually shown by de Pasquale & Mohnke (2014) for targets in the shallow vadose zone. The first field SNMR-PP measurement was conducted on a water reservoir by Lin *et al.* (2018a) with a 2 m square PP-loop and 1200 A effective DC. Quite recently, the application of SNMR-PP for underground tunnel measurements has also attracted interest within the SNMR community (Lin *et al.* 2019; Costabel 2019). Furthermore, although not being a classical hydrogeophysical SNMR application in terms of hydrogeophysical aquifer characterization, the detection of oil under sea ice from a mobile, helicopter-borne NMR device also makes use of pre-polarization techniques to amplify the measured NMR signal (Conradi *et al.* 2018; Altobelli *et al.* 2019).

A typical SNMR-PP measurement sequence is sketched in Fig. 1. Initially a strong PP $\mathbf{B}_p$-field is generated by energizing a PP-loop with a large DC current I_p for a duration long enough to polarize the spins to a known level to enhance the subsequent signal amplitude. The length of the PP-pulse (ms to s) depends on the T_1 relaxation time of the investigated medium as the enhanced magnetization builds up with T_1. After switching-off the PP-field within the switch-off ramp time τ_r, a pulse (Tx) is used to excite the hydrogen protons in the subsurface. Subsequently a NMR response, typically a free induction decay (FID), can be recorded for up to several hundreds of milliseconds depending on the particular relaxation times of the investigation target. By increasing either the length or amplitude of the Tx-pulse, it is possible to excite deeper and larger volumes in the subsurface and therefore gather quantitative, depth-resolved information about water content and relaxation time.

Common to the aforementioned SNMR-PP applications, is the assumption that the PP switch-off itself is carried out properly. This means that the PP-field has to be switched-off (or better ramped down - red line in Fig. 1) in a particular manner during the time span τ_r, so that the enhanced magnetization is perfectly aligned with the Earth's magnetic field at the end of the switch-off. Two important things need to be considered here. Due to its spatial inhomogeneity, the magnitudes of the PP-field range over several orders of magnitude. Furthermore, the spatial distribution of relative orientations between the Earth's magnetic field and the PP-field varies with the inclination of the Earth's magnetic field and locally ranges between 0° and 180°. For practical considerations this means that a particular switch-off ramp (with a fixed switch-off time τ_r) used in a certain SNMR-PP device, needs to be optimized for all combinations of PP-field amplitudes and relative orientations. Considering this rather large parameter space it is very unlikely that the maximal theoretically possible enhanced magnetization is established over

the entire affected subsurface after the PP switch-off (e.g. Melton *et al.* 1995; Melton & Pollak 2002; Conradi *et al.* 2017). Furthermore, when targeting the shallow subsurface (e.g. vadose zone), which features T_1 relaxation times even shorter than about 100 ms, the time span between PP switch-off and FID record should be as short as possible to avoid signal loss due to T_1 relaxation. This time span consists of wait time τ_w, Tx-pulse excitation and dead time τ_d (cf. Fig. 1), where τ_w and τ_d are generally device-dependent and the Tx-pulse length depends on the measurement protocol and/or target depth. Depending on these parameters it may be possible to prolong the switch-off time τ_r to increase the adiabatic switch-off performance. In any case, one needs to evaluate the trade-off between switch-off performance due to longer τ_r and magnetization decrease due to short T_1 relaxation.

The objective of this work is to quantify the effect of an imperfect PP switch-off on the resulting NMR signal due to the application of different PP switch-off ramps. To do so, we use full spin dynamics simulations of the PP-switch-off within the calculation of the 3-D SNMR forward kernel. This means that for every point in the subsurface where the **B**-field is calculated, we need to solve a set of differential equations to determine the magnetization after the PP switch-off. Considering the **B**-field grid discretization (nr × nφ × nz = 71 × 361 × 192) later used in Section 2, the number of points, and hence the number of needed calculations is almost 5 million. If for a given SNMR-PP setup and PP switch-off ramp, the effect of the PP switch-off on the SNMR signal is negligible, one could omit this extensive and time consuming procedure for any further SNMR kernel calculations. The surface loop sizes exemplarily used in this work are $d = 2$ m and are comparable to the sizes used in the works of Lin *et al.* (2018a) and Costabel *et al.* (2019). Consequently, this size roughly holds for any geophysical SNMR-PP setup currently in use and is constrained by the technically applicable DC current that drives the PP-loop (which is in the order of 20–100 A per turn and an effective DC of about 1000 A). If available, we utilize PP switch-off ramp shapes that have been applied by other groups either for geophysical SNMR-PP (Lin *et al.* 2018a; Costabel *et al.* 2019) or alternative applications that also use PP for NMR signal enhancement (Melton *et al.* 1995; Conradi *et al.* 2017). The intention of this work is not to present or propose a particularly optimized switch-off ramp for a certain special application. In contrast, we want to raise the awareness that the non-consideration of the PP switch-off might lead to unexpected and undesired results.

Our study was partially inspired by the works of Melton *et al.* (1995), Melton & Pollak (2002), Conradi *et al.* (2017) and uses some of their results as benchmark cases for our numerical implementation (cf. the Appendix). We like to point out that the application of SNMR-PP significantly differs from the works of the aforementioned groups. While Melton & Pollak (1971), Melton *et al.* (1995) and Melton & Pollak (2002) were using NMR with PP in the Earth's magnetic field to study the relaxation of liquids similar to laboratory NMR relaxometry measurements, Conradi *et al.* (2018) and Altobelli *et al.* (2019) use NMR with PP to qualitatively detect oil on water under a layer of sea ice. Essentially, and in contrast to SNMR, the latter application is a detection method with additional quantification capability. Because SNMR applications always aim to exactly quantify the amount of water in a particular depth-resolved subsurface volume, they need to use the extensive forward modelling described above.

This paper is structured as follows: first, we introduce the basic concepts of SNMR including the difference of OR- and AP-excitation. Then, we show the spatial sensitivity of an ideal enhancement of the SNMR signal due to a perfect PP-pulse switch-off.
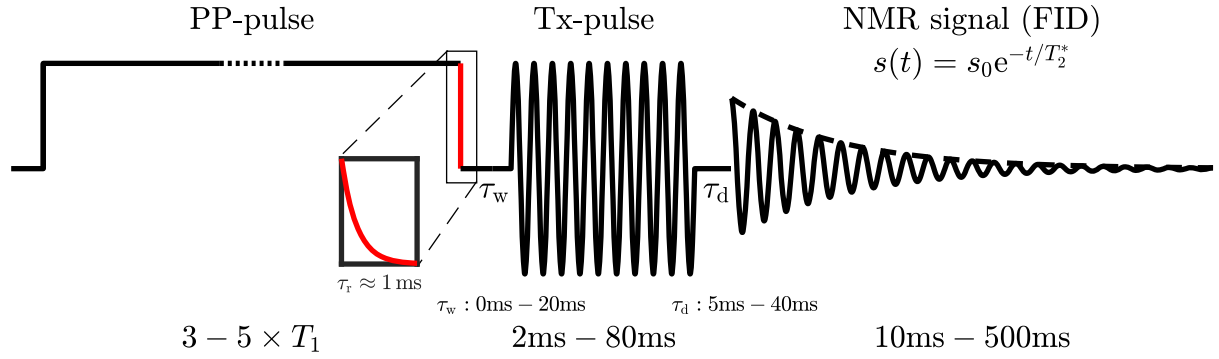
Figure 1. Sketch showing a typical SNMR-PP measurement sequence: PP-pulse with switch-off ramp (red) → wait time τ_w → Tx-pulse (on-resonant or adiabatic) → dead time τ_d → NMR signal response; note that the axes are not to scale.

Subsequently, we focus on the imperfect PP-pulse switch-off and carry out a parameter study to evaluate the dependence of the effectiveness of different switch-off ramps on the control parameters. We finalize the results part by comparing the influence of different switch-off ramps on forward modelled SNMR signal amplitudes.

2 THEORETICAL BASICS OF SNMR

The nuclear spins of hydrogen protons precess around the Earth's magnetic field $\mathbf{B}_0$ (with amplitude $B_0 = |\mathbf{B}_0|$) with the angular Larmor frequency $\omega_L = 2\pi f_L = -\gamma_H B_0$, where γ_H is the gyromagnetic ratio of hydrogen. Note, that the negative sign of the resulting Larmor frequency defines only the direction of precession of the spin and is most of the time safely ignored for common SNMR applications. The spins preferentially align with the axis of $\mathbf{B}_0$ and depending on the magnitude of $\mathbf{B}_0$, this alignment generates a small magnetic moment $\mathbf{M}_0 \propto \mathbf{B}_0$ (e.g. Levitt 2002). In case of SNMR-PP the magnetic moment $\mathbf{M}_0$ is proportional to the resulting field $\mathbf{B} = \mathbf{B}_0 + \mathbf{B}_p$, where $\mathbf{B}_p$ is the magnetic field generated by the PP-loop. In order to stimulate a detectable signal, an electromagnetic Tx-pulse at the Larmor frequency is transmitted through a surface loop to excite the proton spins out of their equilibrium state. Thereby, also $\mathbf{M}_0$ is forced out of its equilibrium orientation by the excitation magnetic field $\mathbf{B}_T$ into an excited state $\mathbf{M}$. After the Tx-pulse is switched-off, the spins, and hence also $\mathbf{M}$, reorient towards their equilibrium orientation parallel to $\mathbf{B}_0$. During this relaxation process $M_\perp$, the component of $\mathbf{M}$ that is perpendicular to $\mathbf{B}_0$, precesses around $\mathbf{B}_0$ at the Larmor frequency and therewith induces a measurable voltage response in a surface receiver (Rx) loop. The received signal decays exponentially with

$$s(q, t) = s_0(q)e^{-t/T_2^*} \cos(\omega_L t + \phi_s) , \tag{1}$$

where s_0 is the initial FID amplitude, T_2^* is the free induction decay time and ϕ_s is the phase of the signal with respect to the transmitted Tx-pulse. By varying the pulse moment $q = I_{ac}\tau$, with Tx-pulse current amplitude I_{ac} and pulse length τ, a 1-D sounding curve can be obtained. The measured amplitudes and relaxation times can be inverted for depth-resolved subsurface water content and pore size information, respectively (e.g. Legchenko & Valla 2002; Müller-Petke & Yaramanci 2010; Müller-Petke *et al.* 2016). The forward operator corresponding to eq. (1) is (Hertrich 2008)

$$s_0(q) = \int K(q, \mathbf{r}) f(\mathbf{r}) d\mathbf{r} , \tag{2}$$

with water content distribution $f(\mathbf{r})$ and sensitivity kernel $K(q, \mathbf{r})$. For the general case of separated Tx- and Rx-loops $K(q, \mathbf{r})$ is given by

$$\begin{aligned} K(q, \mathbf{r}) =\, & 2\omega_L M_0 \sin\left(-\gamma q \left|\mathbf{B}_T^+(\mathbf{r})\right|\right) \\ & \times \left|\mathbf{B}_R^-(\mathbf{r})\right| \cdot e^{i[\zeta_T(\mathbf{r}) + \zeta_R(\mathbf{r})]} \\ & \times \left[\mathbf{b}_R^\perp(\mathbf{r}) \cdot \mathbf{b}_T^\perp(\mathbf{r}) + i\mathbf{b}_0 \cdot \left(\mathbf{b}_R^\perp(\mathbf{r}) \times \mathbf{b}_T^\perp(\mathbf{r})\right)\right] , \end{aligned} \tag{3}$$

where $\mathbf{B}_T^+$ and $\mathbf{B}_R^-$ are the co-rotating and counter-rotating parts of the Tx- and Rx-field, respectively. The exponential term in eq. (3) accounts for phase lags associated with subsurface conductivity structures. The unit vectors $\mathbf{b}_T^\perp$, $\mathbf{b}_R^\perp$ and $\mathbf{b}_0$ in the third row of eq. (3) account for the relative orientations of transmitter, receiver and Earth's magnetic field, respectively.

Two general excitation schemes exist in SNMR. When the Tx-pulse is generated by an alternating current I_{ac} at Larmor frequency ω_L, the excitation is called on-resonant (OR) excitation (Weichman *et al.* 2000). This is the general case for most SNMR applications. More recent approaches use adiabatic fast passage pulses (AP), where the Tx-pulse current I_{ac} and its corresponding frequency are modulated in a particular manner to provide a more homogeneous excitation in the subsurface (Tannùs & Garwood 1997; Grunewald *et al.* 2016). In general $M_\perp$ can be determined for both excitation schemes by solving the Bloch equation $d\mathbf{M}/dt = \mathbf{M} \times \gamma_H \mathbf{B}$ (Bloch 1946). However, in case of OR-excitation one can omit the time consuming calculation of the Bloch equation and use directly the solution in the rotating frame of reference (e.g. Hertrich 2008)

$$M_\perp = \sin\left(-\gamma q \left|\mathbf{B}_T^+(\mathbf{r})\right|\right) = \sin\left(\Theta_T\right) , \tag{4}$$

where the flip angle Θ_T describes the orientation of the magnetization after the Tx-pulse. In case of AP-excitation, the effective Tx-field $\mathbf{B}_{eff}$ is modified by a time dependent extra field due to the frequency modulation (e.g. Grunewald *et al.* 2016). Therefore, we solve the corresponding Bloch equation $d\mathbf{M}/dt = \mathbf{M} \times \gamma_H \mathbf{B}_{eff}$ to obtain $M_\perp$ and use it in eq. (3) for the kernel calculation. In Section 4 and the Appendix, we describe the numerical implementation of the Bloch equation to study PP switch-off ramps. From a numerical perspective there is no difference in using the Bloch equation to determine the magnetization for either the PP- or Tx-pulses.

Before studying the effect of PP on SNMR measurements and for introductory reasons, we first compare the effect of OR- and AP-excitation without additional PP. Figs 2(a+b) exemplarily show
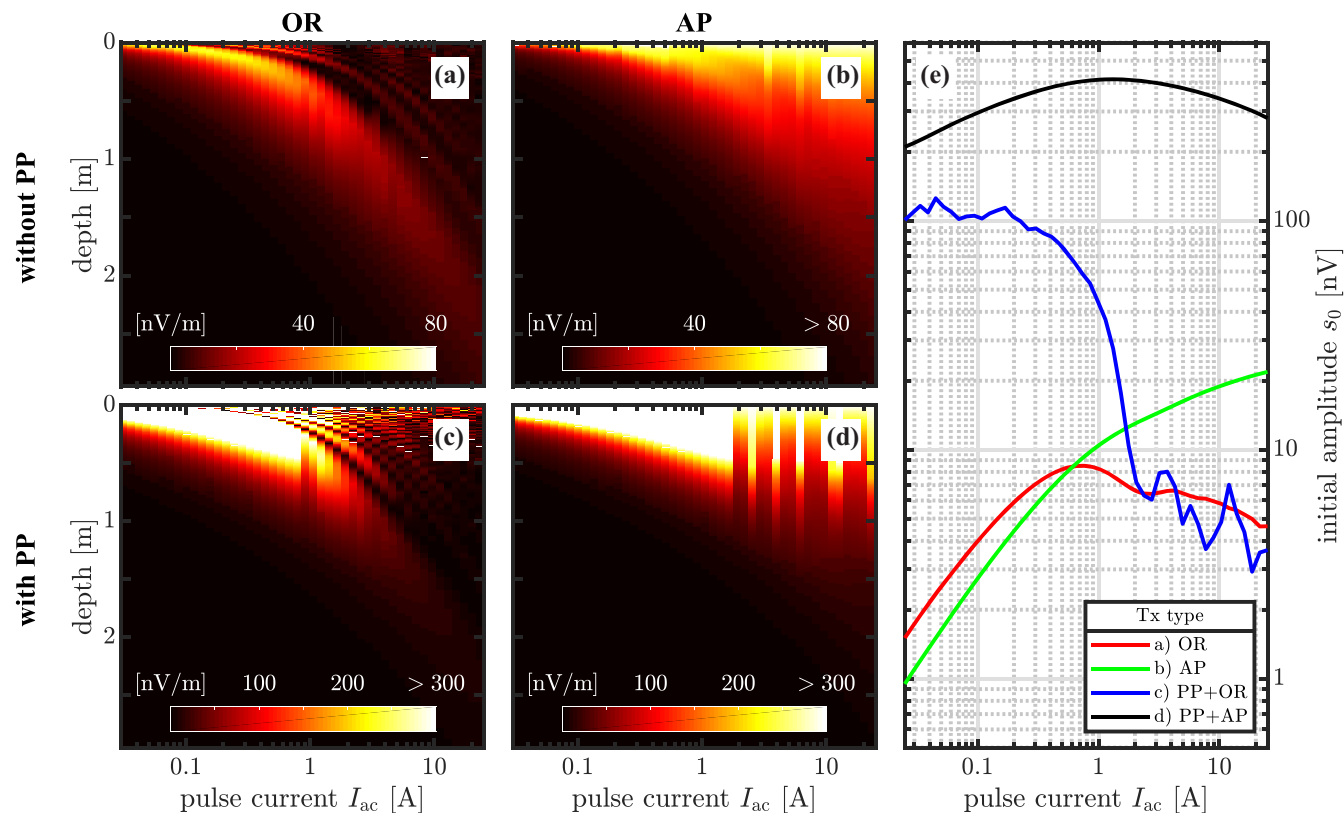
Figure 2. Panels (a–d) sensitivity kernels for two different Tx-excitation pulses – on-resonant OR (left-hand column) and adiabatic half passage AP (right-hand column) either without pre-polarization (top row) or with pre-polarization (bottom row); Note that the colour scale for the PP kernels differs from the kernels without PP; (e) sounding curves calculated from the kernels shown in (a–d) for a homogeneous half space with 30 per cent water content.

the corresponding sensitivity kernels and Fig. 2(e) the associated sounding curves (red and green lines). The kernel calculations were performed with MRSMatlab (Müller-Petke *et al.* 2016) where the magnetic fields are discretized in cylindrical coordinates with number of radial segments nr = 71, number of angular segments nφ = 361 and number of depth layers nz = 192. For both kernels a 100 Ωm half-space and a $d = 2$ m coincident circular loop layout (Tx: 1 turn; Rx: 10 turns) are used. The Earth's magnetic field is set to $B_0 = 48$ μT ($f_L = -2043.7$ Hz) and the pulse length for both pulses is 40 ms. In the AP-case, we use a so-called adiabatic half-passage pulse (Tannùs & Garwood 1997) that sweeps from an offset $\Delta f = -200$ Hz to the Larmor frequency f_L with a hyperbolic tangent. The amplitude modulation for the AP-pulse is given implicitly according to a typical surface NMR coil response with a quality factor of $Q = 30$ (Grunewald *et al.* 2016). The pulse current I_{ac} in Fig. 2 refers to the constant AC current in the OR-case and to the maximum current at the end of the Tx-pulse in the AP-case. The OR-kernel (Fig. 2a) shows the typical banded sensitivity structure, where an increase in I_{ac} yields a corresponding deeper depth focus. Here, the deepest band represents the first perfect excitation, that is a flip angle of 90°. In contrast to this, the AP-kernel (Fig. 2b) exhibits a more homogeneous sensitivity structure that has its maximum close to the surface. The sensitivity structure of both kernels also gets reflected in the corresponding sounding curves. Both sounding curves are calculated for a constant water content of 30 per cent. For smaller pulse currents $I_{ac} < 0.5$ A, the OR sounding curve (red) has larger amplitudes compared to the AP-case (green). For larger I_{ac} and due to the increasing homogeneous excitation with depth, the AP-amplitudes increase up to a factor of 4 compared to the OR-values at similar I_{ac}. For a more detailed

discussion on the implementation of AP-excitation in SNMR and its particular characteristics we refer the reader to Grunewald *et al.* (2016).

3 SNMR-PP WITH PERFECT PRE-POLARIZATION SWITCH-OFF

To further increase the net magnetic moment $\mathbf{M}_0$, and thereby increase the detectable signal amplitude, it is possible to temporarily apply a strong pre-polarizing magnetic field $\mathbf{B}_p$ prior to the actual excitation pulse (Packard & Varian 1954). During the presence of the PP-field $\mathbf{B}_p$, the spins will align with the resulting field $\mathbf{B} = \mathbf{B}_0 + \mathbf{B}_p$ and hence, the magnetic moment $\mathbf{M}_0$ will increase to the spatially varying $\mathbf{M}_p(\mathbf{r}) \propto |\mathbf{B}_0 + \mathbf{B}_p|$ (Melton & Pollak 1971; Planinšič *et al.* 1994; Callaghan *et al.* 1997; de Pasquale & Mohnke 2014). Switching off the polarizing field $\mathbf{B}_p$ adiabatically, causes the spins to reorient towards $\mathbf{B}_0$ and at the same time $\mathbf{M}_p$ exponentially decreases towards $\mathbf{M}_0$ with relaxation time constant T_1 (cf. eq. 6). In case of an adiabatic switch-off, $\mathbf{M}_p$ is perfectly aligned with $\mathbf{B}_0$ after $\mathbf{B}_p$ has vanished and M_0 in eq. (3) can be replaced by M_p to calculate the forward kernel. The adiabatic condition is satisfied if the frequency $\gamma |\mathbf{B}(t)|$ remains much larger than the rate of reorientation of $\mathbf{B}$ from $\mathbf{B}_p$ towards $\mathbf{B}_0$ (Melton *et al.* 1995; Melton & Pollak 2002)

$$\gamma |\mathbf{B}(t)| \gg \frac{d\alpha}{dt} , \qquad (5)$$

where α is the angle between $\mathbf{B}$ and $\mathbf{B}_0$ (cf. Fig. A1a), for the entire duration of the switch-off. To get the maximum yield out of PP, two

things need to be considered when switching off the polarizing field $\mathbf{B}_p$. First, the adiabatic condition itself (eq. 5) has to be satisfied, meaning that the switch-off has to be slow enough, so that $\mathbf{M}_p$ is 'locked' to $\mathbf{B}$ as it decreases in amplitude and reorients to $\mathbf{B}_0$ (Melton *et al.* 1995; Melton & Pollak 2002). If the switch-off is too fast, most of the magnetization will not follow the reorienting $\mathbf{B}$ and will not be aligned in parallel to $\mathbf{B}_0$ at the end of the switch-off. Consequently, these magnetization components do not get coherently excited by a subsequent Tx-pulse and hence, do not contribute to the recorded NMR signal. Secondly, the switch-off has to be fast enough (much faster than T_1) to get the maximum gain out of the increased $\mathbf{M}_p$. If the switch-off is not much faster than T_1, then a considerable amount of magnetization will decay due to T_1-relaxation before the actual Tx-pulse is applied. The critical part when switching off $\mathbf{B}_p$ is at the end of the switch-off when $\mathbf{B}_p$ becomes small and the precession frequency of $\mathbf{M}$ around $\mathbf{B}_0$ is small compared to the rate of change of reorientation of $\mathbf{B}$. This reorientation rate needs to slow down in order to maintain the inequality in eq. (5).

Due to technical limitations of current available SNMR-PP devices and depending on the length of the Tx-pulse, it can take about 50 ms after the PP switch-off until the actual NMR signal is recorded (cf. Fig. 1). Therefore, it is undesirable to have a long PP switch-off (long in respect to the relatively short T_1) that adds magnetization losses due to T_1-relaxation. Reported switch-off times for recent SNMR-PP devices are about 1 ms (Lin *et al.* 2018a,b; Costabel *et al.* 2019) and are therefore about two to three orders of magnitude smaller than typical T_1-values for saturated porous media.

Fig. 3(a) exemplarily shows the amplitudes $B_p = |\mathbf{B}_p|$ in units of the Earth's magnetic field B_0 for a central slice (oriented S→N) out of a 3-D domain. The corresponding PP-field is generated by a 2 m circular PP-loop with $I_p = 1000$ A energizing DC. Only in the very close vicinity of the PP-loop (vertical triangles), B_p exceeds values of 100 (dark red colours). With increasing distance, B_p rapidly decreases to 1 (light blue colours) at about 2 m away from the loop. Because we use an inclination of 60° for the Earth's magnetic field $\mathbf{B}_0$ and due to the inhomogeneity of the PP-field, there is a spatially varying distribution of angles θ that describe the relative orientation of $\mathbf{B}_p$ in relation to $\mathbf{B}_0$ (Fig. 3b). In the case of perfect adiabatic switch-off and neglecting T_1-relaxation, the PP-field in Figs 3(a)+(b) generates an enhanced magnetization M_p as shown in Fig. 3(c). Due to the inclination of $\mathbf{B}_0$ with respect to the PP-loop, the spatial distribution of M_p is not symmetric in the given 2D-plane. The maximum enhancement exceeds 100 close to the PP-loop (yellow) and is even smaller than 1, at greater distances from the PP-loop (dark blue colours), especially to the south.

To visualize the effect of SNMR-PP, we plot two sensitivity kernels in Figs 2(c)+(d) (bottom row) and their corresponding sounding curves in Fig. 2(e). The model parameters are identical to the cases without PP and the applied PP-field corresponds to the one shown in Fig. 3(a). Note that with PP, the colour bar values in Figs 2(c)+(d) are larger compared to the cases without PP. For visualization purposes we combined all values larger than 300 nV m^{-1} into the colour white. For a few points very close to the surface, the sensitivity exceeds 30 000 nV m^{-1} for the cases with PP.

For both SNMR-PP-cases, the sounding curve amplitudes for small I_{ac} are about two orders of magnitude larger compared to the cases without PP. For the PP+OR-case (blue) the amplitudes quickly decrease for $I_{ac} > 0.25$ A and reach values comparable to the ones without PP at about $I_{ac} = 2.5$ A. The fluctuations of the PP+OR sounding curve at larger I_{ac} compared to the OR-case are

notable and attributed to the strong fluctuations of the sensitivity kernel very close to the surface that get traced through even for larger I_{ac}. These fluctuations were already reported by de Pasquale & Mohnke (2014) and are due to the particular loop layout. When spins get excited in regions where the $\mathbf{B}_p$-field is large (close to the loop), the flip angle Θ_T can get larger than 180° and the amplitude contribution of those regions is negative, hence the oscillating kernel. To suppress these oscillations, the authors suggested to decrease the size of the Tx/Rx-loops by a factor of three compared to the size of the PP-loop. However, as this would also decrease the maximum possible enhancement and penetration depth, we have chosen to use the aforementioned coincident loop layout. The PP+AP sounding curve (black) shows a different behavior. For small I_{ac} values the amplification is even higher than for the PP+OR-case (different to the cases without PP). Similarly to the AP-case (green), the amplitudes of the PP+AP signal initially increase up to about $I_{ac} = 1$ A. Although the amplitudes slightly decrease again for larger I_{ac}, they are still more than one order of magnitude higher compared to the AP-case without PP. Due to the much more homogeneous AP-excitation the undesirable kernel oscillations have also vanished.

Both SNMR-PP-kernels show a high sensitivity at the shallow subsurface (bright yellow and white colours) due to the large $\mathbf{B}_p$-field magnitudes close to the PP-loop and the strong decreasing effect of the $\mathbf{B}_p$-field with increasing depth (cf. also Fig. 3a). This basic comparison demonstrates the advantages of SNMR-PP for shallow subsurface measurements in terms of signal enhancement, especially when combined with AP-excitation.

4 SNMR-PP WITH IMPERFECT PRE-POLARIZATION SWITCH-OFF

Now, we want to study the effect of an imperfect PP switch-off on the enhancement of the final NMR signal. But before doing so, we compare different switch-off ramps and how the particular ramp shape and ramp time τ_r influence the switch-off characteristics. In order to reliably quantify a spatially varying subsurface water content distribution it is essential to determine the actual magnetization $\mathbf{M}_p$ after the switch-off. Considering the practical applicability of SNMR-PP devices, we need to evaluate to what extent a particular switch-off ramp influences the recorded NMR signal. Here, our objective is not to propose or develop a particular switch-off ramp but rather to familiarize the reader with the consequences that may arise when using one of the presented ramps.

To evaluate different PP switch-off ramps, we need to study the full NMR spin dynamics of the magnetization $\mathbf{M}_p$ during the switch-off of the $\mathbf{B}_p$-field. To this end, we developed the software BLOCHUS (Bloch Universal Simulator), a set of Matlab™ tools including a graphical user interface (GUI) that implements the governing equation of motion, the Bloch equation (Bloch 1946), in a laboratory frame of reference

$$\frac{d\mathbf{M}_p}{dt} = \gamma \mathbf{M}_p \times [\mathbf{B}_0 + \mathbf{B}_p] - \frac{M_{p,x}\mathbf{e}_x + M_{p,y}\mathbf{e}_y}{T_2}$$
$$- \frac{(M_{p,z} - M_0)\mathbf{e}_z}{T_1}, \tag{6}$$

with longitudinal and transversal relaxation times T_1 and T_2. By controlling the amplitude of the PP-current $I_p(t)$ during switch-off, any arbitrary ramp shape and its corresponding effect on $\mathbf{B}_p$, and hence $\mathbf{M}_p$, can be modelled. Internally, BLOCHUS solves eq. (6)
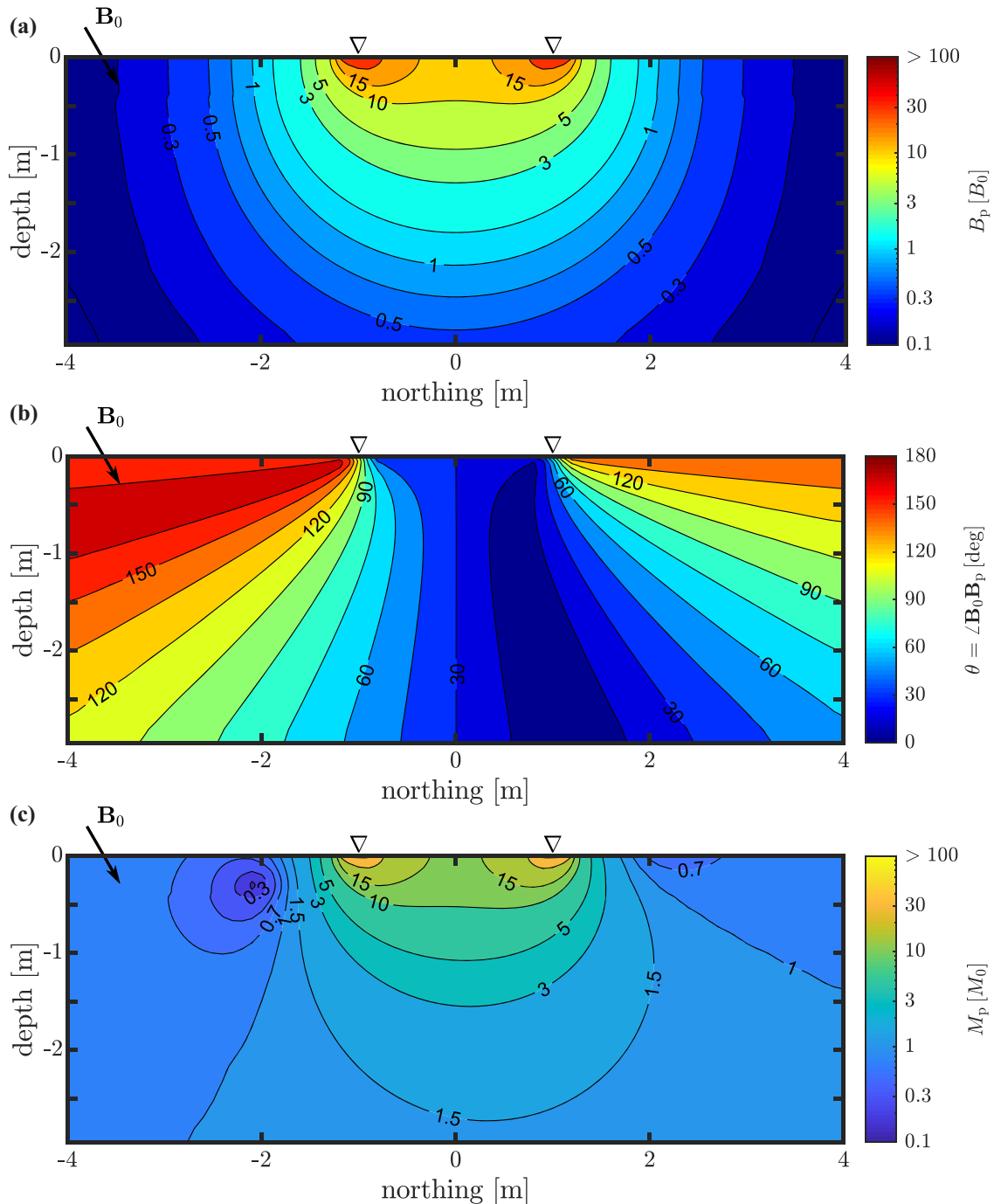
Figure 3. Panel (a) amplitudes $B_p = |\mathbf{B}_p|$ of a PP-field generated by a circular PP-loop with $d = 2$ m and effective DC of $I_p = 1000$ A; (b) angle θ between $\mathbf{B}_0$ and $\mathbf{B}_p$; (c) corresponding amplitudes $M_p = |\mathbf{M}_p|$ of the amplified magnetization after a perfectly adiabatic switch-off of the $\mathbf{B}_p$-field shown in (a); all sub panels are 2-D slices out of a 3-D domain and are oriented S→N; the vertical triangles in all sub panels indicate the PP-loop position.

with Matlab's 'ode45' routine, which uses a fifth-order Runge–Kutta method with adaptive time stepping (Shampine & Reichelt 1997). To use the extensive modelling capabilities of MRSmatlab (Müller-Petke *et al.* 2016), BLOCHUS also contains an interface to the kernel calculation routines provided by MRSmatlab. As mentioned above and without loss of generality, eq. (6) can also be used to model the magnetization $\mathbf{M}$ during a Tx-pulse (either OR or AP) and therewith implicitly consider effects like relaxation during pulse (Grombacher *et al.* 2017). In the Appendix, we provide two benchmark scenarios to validate our implementation of eq. (6).

4.1 Parameter study

As we have shown in Figs 3(a)+(b), the amplitudes B_p and the relative orientation θ strongly vary in magnitude and spatial extent. Therefore, and depending on the shape and duration of the switch-off ramp, the PP switch-off is not perfect in every point of the subsurface volume. To quantify this, we determine the 'adiabatic quality' p as a function of amplitude B_p and angle θ for various switch-off ramps (cf. Fig. 4). Herein, $p = \mathrm{proj}_{\mathbf{B}_0} \mathbf{M}_p$ is the normalized projection of the magnetization $\mathbf{M}_p$ onto the final magnetic
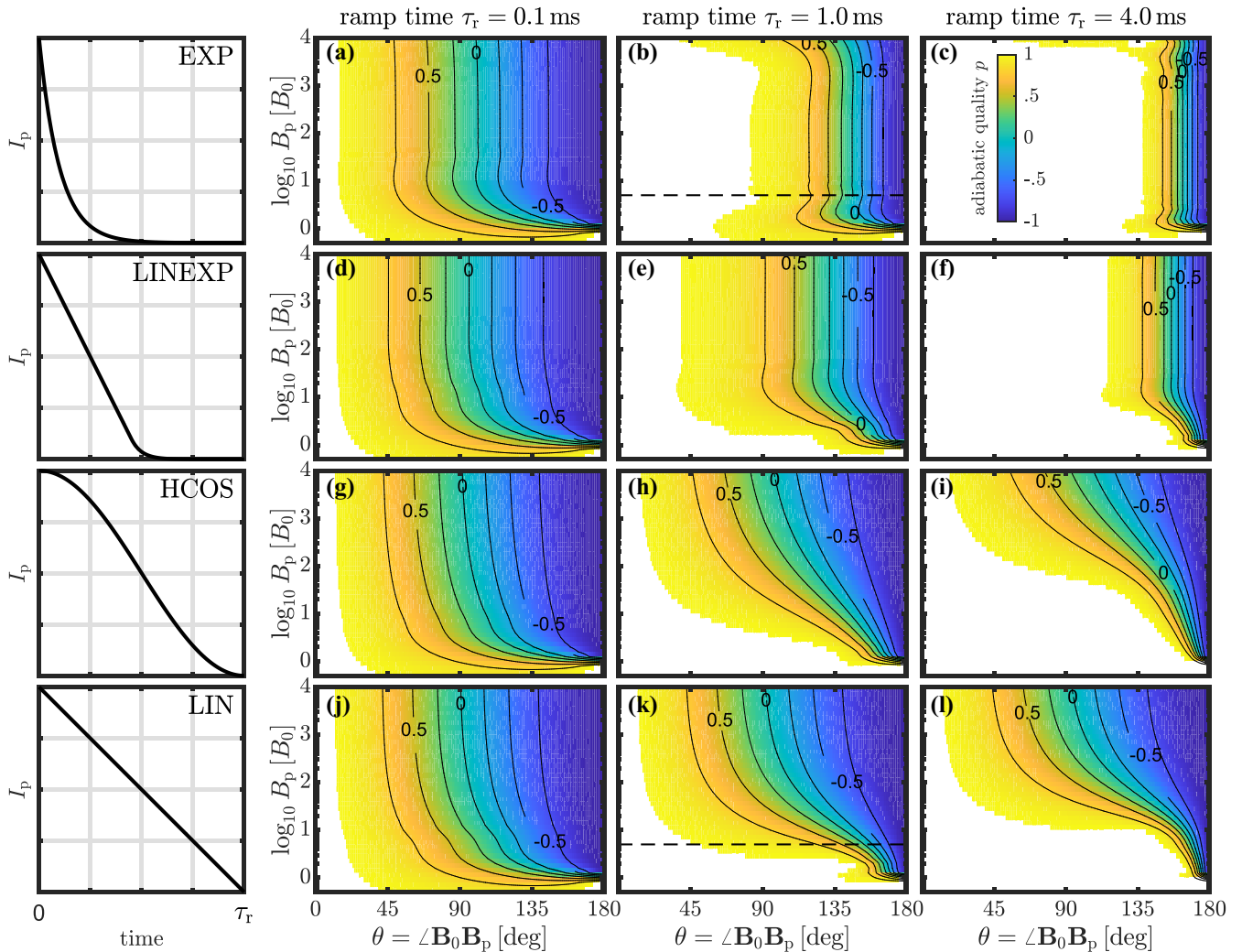
Figure 4. Adiabatic quality p as a function of B_p and angle θ for four different ramp shapes (rows) and three different switch-off times τ_r (columns); $p = 1$ (white) indicates perfect adiabatic switch-off.

field $\mathbf{B} = \mathbf{B}_0$ after the switch-off (Conradi *et al.* 2017). The case $p = 1$ describes the ideal case, that is $\mathbf{M}_p$ and $\mathbf{B}_0$ are perfectly parallel after switch-off and the full magnitude of $\mathbf{M}_p$ can get excited by a subsequent Tx-pulse. The values $p = 0$ and $p = -1$ cover the perpendicular and anti-parallel case, respectively and would lead to a decreased Tx-excitation. In the following, we will use p as an effective measure to evaluate the quality of the PP switch-off.

We exemplarily use four different ramp shapes:

(i)   EXP – exponential (Lin *et al.* 2018a,b)
(ii) LINEXP – linear & exponential (e.g Conradi *et al.* 2017)
(iii) HCOS – half cosine (Costabel *et al.* 2019)
(iv) LIN – linear (e.g Melton *et al.* 1995)

which have been published before and are partly in use in current SNMR-PP devices. Each ramp shape was calculated for three different switch-off times τ_r of 0.1, 1 and 4 ms where the ramp time τ_r is defined as the total time span that is used to ramp the $\mathbf{B}_p$-field down to zero. Note that similar to a real SNMR-PP measurement, τ_r is fixed for all combinations of B_p and θ within the corresponding column of Fig. 4. For all calculations we neglected T_1- and T_2-relaxation.

With the chosen set of ramp shapes and ramp times, we cover a reasonable range of parameters for technical applicable SNMR-PP measurements. A ramp time of $\tau_r = 1$ ms is reported in Lin *et al.* (2018b) and Costabel *et al.* (2019) and the two other ramp times serve as 'boundary' cases to evaluate the dependence of p onto τ_r. We note that the short ramp time of $\tau_r = 0.1$ ms might be challenging to implement in a real SNMR-PP device, especially when considering the strong currents involved. The ramp shapes are chosen to cover a range of shapes that show distinct differences at early and late times, respectively. Considering the adiabatic criterion in eq. (5), obviously using the EXP-ramp seems to be a generally favourable choice as it releases a lot of energy over a short period of time (and early) while it significantly slows down at later ramp times. On the contrary, the HCOS-ramp releases the energy much more slowly and uniformly and will therefore violate eq. (5) over a larger period of time. However, as this ramp is also in practical use, we want to evaluate its effect on the switch-off quality. The other two shapes are the benchmark cases from the Appendix, where for the cases presented here the switch-over field strength for the LINEXP-ramp is fixed to $B^* = B_p/10$. In Fig. 4 the adiabatic quality p is colour coded from white ($p = 1$, perfect adiabatic switch-off) over yellow, green ($p = 0$) to blue ($p = -1$).

By basic inspection of the p-distributions in Fig. 4, several features can be recognized. First and in line with the adiabatic criterion in eq. (5), for each ramp shape (rows in Fig. 4) the global adiabatic quality increases with increasing ramp time τ_r. By 'global' we refer to the whole range of B_p and θ values considered here. However, the increase of the global adiabatic quality itself with increasing τ_r is significantly different for the individual ramp shapes. For the case of $\tau_r = 0.1$ ms there seems to be no significant difference between the individual ramp shapes. In this particular case, all ramp shapes show an equally poor performance when compared to corresponding results for longer ramp times. Within the relevant PP-parameters, a switch-off time of 0.1 ms is simply too fast to allow for an adiabatic reorientation if the initial angle between $\mathbf{B}_p$ and $\mathbf{B}_0$ is already larger then $\theta \approx 45°$. For a ramp time of $\tau_r = 1$ ms the global adiabatic quality p shows a distinct dependence on the ramp shape. For the EXP-ramp, the switch-off is perfect up to an angle of $\theta \approx 115°$ (Fig. 4b). For the LINEXP, the HCOS and the LIN ramps this onset of low adiabatic quality happens continuously 'earlier' at smaller angles θ (Figs 4e, h and k). Furthermore, while for the EXP-ramp the distribution of p is rather independent on the magnitude of B_p, the dependence on B_p is continuously increasing for the LINEXP, the HCOS and the LIN ramps. For the latter ones, the global adiabatic quality increases with decreasing B_p. The results for $\tau_r = 4$ ms are along the same line of arguments as for the results for $\tau_r = 1$ ms. The main difference is that a high adiabatic quality can be achieved over a larger range of θ values. These findings seem to confirm that for a large range of B_p and θ values, the EXP-ramp outperforms the LINEXP, HCOS and LIN ramps and therefore should yield the maximum PP-effect in a real SNMR-PP measurement.

To further evaluate these results in regard of a real SNMR-PP measurement, we calculate the spatial distribution of adiabatic quality p for the EXP and LIN-ramps with $\tau_r = 1$ ms as they differ most significantly from each other in terms of global p at this particular τ_r (cf. Fig. 4). We use the amplitudes B_p and angles θ from the PP-field presented in Figs 3(a)+(b) and determine $\mathbf{M}_p$ and therewith also p based on the Bloch equation eq. (6). Fig. 5 shows the corresponding central slices of the 3-D distribution of p when either an EXP-ramp (Figs 5a+b) or LIN-ramp (Figs 5c+d) is used. For each ramp, we determine p for two different inclinations: 60° (Figs 5a+c) and −60° (Figs 5b+d). This not only illustrates the spatial variability of the switch-off quality depending on the relative orientation of $\mathbf{B}_0$ and $\mathbf{B}_p$, but once more demonstrates that it might be necessary to account for these effects already in the forward calculation.

Despite the general better global performance of the EXP-ramp compared to the LIN-ramp (cf. Fig. 4), this ramp yields a larger volume of low p-values (Fig. 5). By a detailed evaluation of Figs 3, 4+5 it becomes apparent that for values smaller than about $B_p < 5$ (dashed line in Fig. 4b+k), the LIN-ramp (Fig. 4k) shows indeed a higher adiabatic quality over a wider range of angles θ compared to the EXP-ramp (Fig. 4b). Whereas for amplitudes $B_p > 10$, the adiabatic quality of the LIN-ramp significantly decreases. This can be seen, for example in Fig. 5(c) below and inside the loop where the p-values are smaller than 1. For the case of −60° inclination (Figs 5b+d) the situation is similar to the one described before. The total volume of reduced p-values is larger for the EXP-ramp than for the LIN-ramp. Additionally, due to the reversed inclination a large amount of magnetization is oriented antiparallel below the center of the loop. In this case a substantial amount of magnetization would not contribute to the NMR signal. A simple way to deal with this kind of situation is to reverse the direction of the PP-current (Conradi *et al.* 2017) and therewith establish the p-distribution as shown for the 60° inclination case (Figs 5a+c). However, depending

on the particular inclination of the Earth's magnetic field, there will be points in the subsurface where $p < 1$ and therefore also the usable magnetization M_p will be reduced correspondingly.

4.2 Effect of imperfect switch-off on SNMR-PP sounding curves

So far, we have shown that an imperfect, that is non-adiabatic, switch-off has a considerable effect on the spatial distribution of p and that it strongly depends on the particular PP switch-off ramp. However, a meaningful insight into this effect can only be gained by quantifying it in terms of signal strength of the SNMR-PP sounding curve. To this end, we use the SNMR-PP scheme with AP-excitation pulses as introduced in Section 3. This yields the largest signal enhancement regarding our measurement configuration and additionally also suppresses the unwanted kernel oscillations if instead used with OR-excitation (cf. Fig. 2). In order to calculate sounding curves similar to the ones in Fig. 2(e), we replace the equilibrium magnetization M_0 in eq. (3) with the component of $\mathbf{M}_p$ that is parallel to $\mathbf{B}_0$ after the switch-off. Remember that only magnetization components parallel to $\mathbf{B}_0$ get coherently excited by a subsequent Tx-pulse and result in a measurable NMR signal. All presented sounding curves use the same modelling parameters as described in Section 3 for the PP+AP case. In practice this means that for every sounding curve, we use a particular fixed ramp shape and ramp time combination and calculate the 3-D distribution of enhanced magnetization $\mathbf{M}_p$ that is established after the PP switch-off. The magnetization $\mathbf{M}_p$ gets excited by an AP Tx-pulse and the corresponding voltage response is recorded in a Rx-loop at the surface. The initial values of this recorded NMR-signal are plotted as a function of final Tx-pulse current I_{ac} in Fig. 6. In addition and to focus on the signal loss due to the particular ramp parameters, we normalize all curves with the PP+AP-case with theoretically perfect adiabatic switch-off (Fig. 2b black curve). This means the closer the amplitude of a curve in Fig. 6 is to $s_0^{ramp}/s_0^{ideal} = 1$, the more adiabatic is the switch-off and the better is the signal enhancement compared to the ideal case.

Fig. 6 shows sounding curves corresponding to the EXP and LIN ramps with solid and dashed lines, respectively. Colour coded are the different switch-off ramp times of the corresponding ramp. Let us first consider the case for 60° inclination (Fig. 6a). For a switch-off time of $\tau_r = 1$ ms (red) the EXP-ramp sounding curve retains about 83 per cent signal amplitude compared to the perfect case over the entire Tx-pulse current range. For the LIN-ramp on the other hand, the amplitude loss is much more dramatic with only 15 per cent (low I_{ac}) to 55 per cent (high I_{ac}) compared to the perfect case. The large difference between the two sounding curves partly originates from the individual switch-off performance of the corresponding ramp at large PP-field strengths present inside/below the PP-loop (cf. Figs 4b+k) and partly from the high sensitivity at the shallow subsurface for this particular loop layout and AP-excitation (cf. Fig. 2a bottom right). Although the volume having reduced p-values is larger for the EXP-ramp (cf. Fig. 5), the resulting sounding curve deviates much less from the perfect case compared to the LIN-ramp. This is due to the better performance of the EXP-ramp for larger B_p amplitudes at smaller angles θ (cf. Fig. 4) within the sensitive region of the Tx/Rx-loops. For a very short ramp time of $\tau_r = 0.1$ ms (black), both sounding curves retain less then 40 per cent of the signal amplitude over the entire range of Tx-pulse currents. For a longer ramp time of $\tau_r = 4$ ms (blue) the EXP-ramp retains more than 98 per cent of the signal amplitude of the perfect case. Even
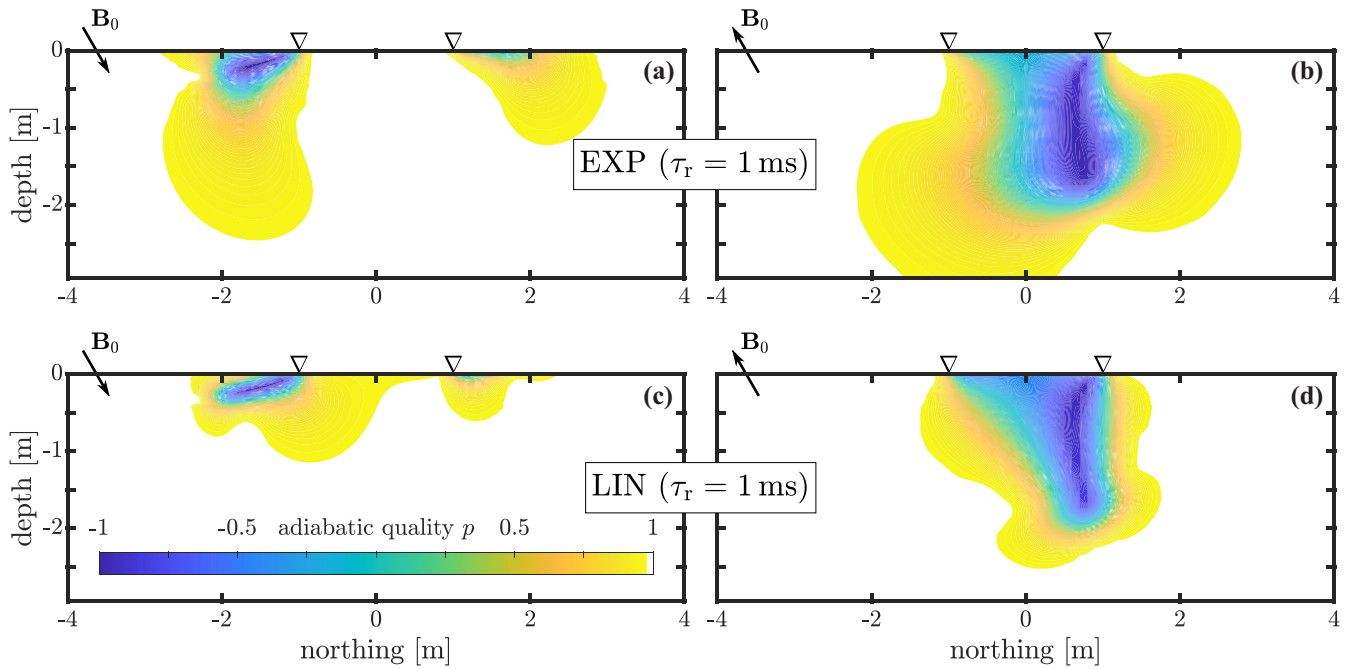
Figure 5. Spatial distribution of adiabatic quality p for the EXP (a+b) and LIN (c+d) switch-off ramps with a switch-off time of $\tau_r = 1$ ms; In (a+c) the inclination is $60°$ and in (b+d) the inclination is $-60°$; all sub panels are 2-D slices out of a 3-D domain and are oriented N→S; the vertical triangles in all sub panels indicate the PP-loop position.
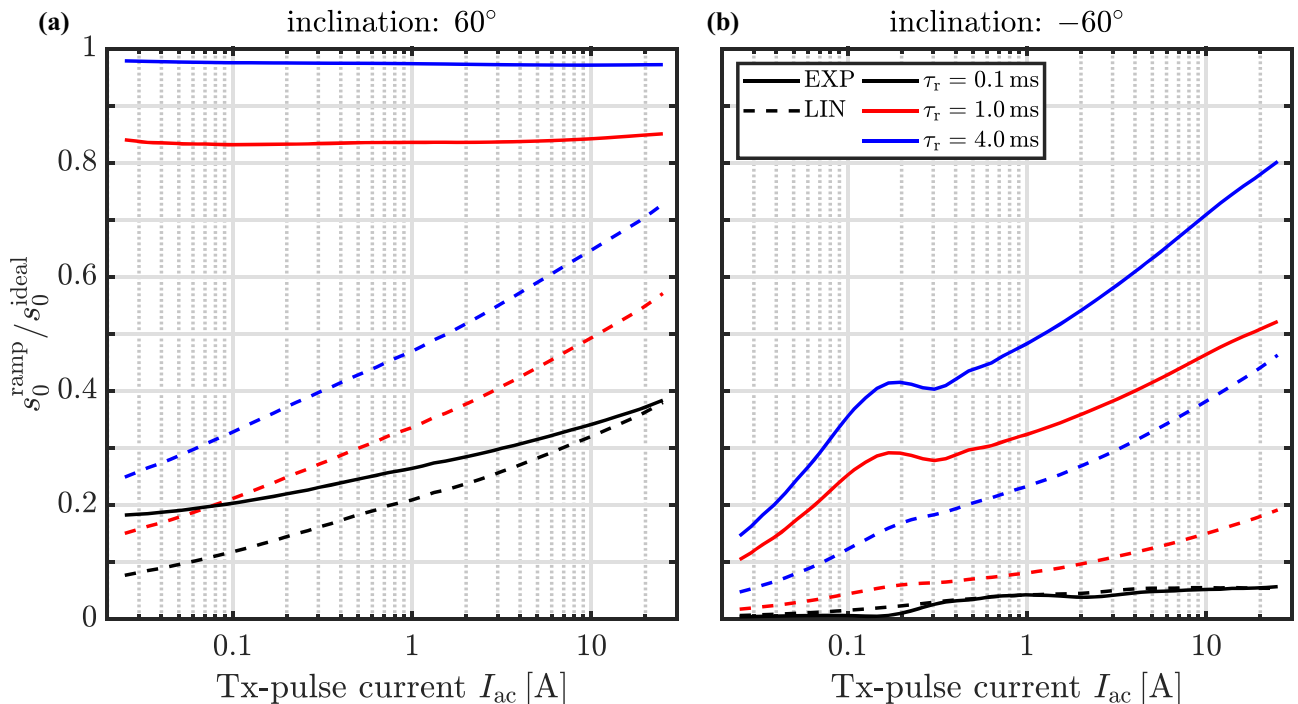

Figure 6. Normalized sounding curves as a function of Tx-pulse current I_{ac} for the EXP (solid) and LIN (dashed) switch-off ramps for three different switch-off times τ_r (colours); all sounding curves are normalized by the PP+AP sounding curve with perfect adiabatic switch-off (cf. Fig. 2b); In (a) the inclination is $60°$ and in (b) the inclination is $-60°$.

for this quite long switch-off time, the LIN-ramp achieves only an average value of about 50 per cent. For the LIN-ramp, the signal loss at small Tx-pulse currents (close to the surface and hence closer to the PP-loop) is stronger than for larger Tx-pulse currents, which is again attributed to the poor performance at large values of B_p (cf. Fig. 4) compared to the EXP-ramps. In this comparison we left

out the LINEXP and HCOS ramps for visibility reasons and because we want to put focus on the qualitative differences. The sounding curves for both of these ramps plot between the sounding curves for the EXP and LIN ramps for every ramp time we considered. The results for $-60°$ inclination impressively show how severe the effect of the relative orientation of the magnetic fields is. Even for a long

switch-off time of $\tau_r = 4$ ms the signal amplitude of the EXP-ramp at small I_{ac} is reduced to less than 30 per cent. Furthermore, all sounding curves show a strong dependence on I_{ac}, where for larger I_{ac} the performance generally increases.

It is not surprising that ramps which fulfill the adiabatic condition much better during switch-off (EXP, LINEXP) perform much better than, for example the HCOS and LIN ramps. The observed differences between the individual ramps might be significantly decreased for loop layouts where the Tx/Rx-loops are placed in a particular manner, so that their sensitive region is further away from the PP-loop and the relative orientations between $\mathbf{B}_0$ and $\mathbf{B}_p$ are more favourable. However, this always comes at the cost of reduced magnetization enhancement and penetration depth (de Pasquale & Mohnke 2014). The cases presented here, should therefore be regarded as a kind of worst case scenarios in terms of underestimating the NMR signal amplitude if the particular PP switch-off ramp is not considered in the forward calculation. More importantly, any signal loss, as presented in Fig. 6, is directly misinterpreted as reduced water content when performing the inversion of the SNMR-PP data.

5 SUMMARY AND CONCLUSIONS

The combined use of PP and AP is a promising approach to significantly enhance the signal quality of SNMR measurements that target shallow subsurface water content distributions. The nowadays available SNMR-PP devices allow investigations down to depths of about 2 m depending on loop size and available PP-current. A typical SNMR-PP excitation consists of a strong PP-pulse that aligns the enhanced magnetization with the prevailing magnetic field. After the PP-field is switched off adiabatically, the magnetization aligns with the Earth's magnetic field and gets excited by a subsequent Tx-pulse. In theory, the amplified magnetization is properly aligned with the Earth's magnetic field at the end of the PP switch-off. Due to the inhomogeneity of the PP-field and the generally fixed settings of the particularly used PP switch-off ramp, there are always regions in the subsurface where the PP switch-off is non-adiabatic, that is imperfect. The spatial distribution of these imperfect regions mainly depends on the relative orientation between the Earth's magnetic field and the PP-field and therefore of course implicitly on the inclination of the Earth's magnetic field.

To quantify the effect of an imperfect PP switch-off on SNMR-PP signals, we developed a numerical scheme that allows to study arbitrary ramp shapes and incorporates the PP switch-off simulation directly into the well-established SNMR modelling framework MRSmatlab. For parameters typically used in current SNMR-PP applications the enhancement performance varied between 15 and 83 per cent of the perfect PP-case, depending on the chosen ramp parameters and Tx-pulse current (cf. Fig. 6). This is particularly interesting because until now, all SNMR-PP modelling studies assume adiabatic, that is perfect, switch-off conditions for the PP-field (de Pasquale & Mohnke 2014; Lin *et al.* 2018a,b; Lin *et al.* 2019). Depending on the severity of the performance loss, this effectively leads to an underestimation of the inverted water content.

The presented modelling framework directly incorporates the PP switch-off into the SNMR-PP forward calculation. This allows to correctly account for the PP switch-off in already available SNMR-PP devices. Furthermore, it enables the user to evaluate and optimize different PP/Tx/Rx-loop layouts and PP/Tx-excitation parameters during the development of a new generation of SNMR-PP devices. Inherently, the performance of any switch-off ramp will depend

on the available power electronics of the particular SNMR-PP device. Regarding the maximal possible magnetization enhancement, it seems advantageous to use exponentially shaped ramps that fulfill the adiabatic condition almost during the entire switch-off time. However, in our opinion a generalization on the optimal switch-off ramp shape and time is difficult to make and depends on the particular application. Our future work will focus on the development of optimal PP/Tx/Rx measurement setups and parameters, in order to qualitatively and quantitatively target shallow subsurface water content distributions.

REFERENCES

Altobelli, S.A. *et al.*, 2019. Helicopter-borne NMR for detection of oil under sea-ice, *Mar. Pollut. Bull.,* **144,** 160–166.

Behroozmand, A., Keating, K. & Auken, E., 2015. A review of the principles and applications of the NMR technique for near-surface characterization, *Surv. Geophys.,* **36**(1), 27–85.

Bloch, F., 1946. Nuclear Induction, *Phys. Rev.,* **70**(7–8), 460–474.

Callaghan, P.T., Eccles, C.D. & Seymour, J.D., 1997. An earth's field nuclear magnetic resonance apparatus suitable for pulsed gradient spin echo measurements of self-diffusion under Antarctic conditions, *Rev. Sci. Instrum.,* **68**(11), 4263–4270.

Conradi, M.S., Altobelli, S.A., Sowko, N.J., Conradi, S.H. & Fukushima, E., 2017. Pre-polarization fields for earth's field NMR: Fast discharge for use with short T1 and large coils, *J. Magnet. Reson.,* **281**(Supplement C), 241–245.

Conradi, M.S., Altobelli, S.A., Sowko, N.J., Conradi, S.H. & Fukushima, E., 2018. Earth's field NMR detection of oil under arctic ice-water suppression, *J. Magnet. Reson.,* **288**, 95–99.

Costabel, S., 2019. Noise analysis and cancellation for the underground application of magnetic resonance using a multi-component reference antenna - case study from the rock laboratory of Mont Terri, Switzerland, *J. appl. Geophys.,* **169,** 85–97.

Costabel, S. & Müller-Petke, M., 2014. Despiking of Magnetic Resonance Signals in time and wavelet domain, *Near Surf. Geophys.,* **12,** 185–197.

Costabel, S., Siemon, B., Houben, G. & Günther, T., 2017. Geophysical investigation of a freshwater lens on the Island of Langeoog, Germany–insights from combined HEM, TEM and MRS data, *J. appl. Geophys.,* **136,** 231–245.

Costabel, S., Hiller, T., Radic, T., Dlugosch, R. & Müller-Petke, M., 2019. Surface nuclear magnetic resonance measurements in Berlin - proof-of-concept for applying the prepolarisation technique in urban areas, in *Conference Proceedings of the 25th European Meeting of Environmental and Engineering Geophysics,* Vol. **2019,** pp. 1–5, European Association of Geoscientists & Engineers.

de Pasquale, G. & Mohnke, O., 2014. Numerical study of prepolarized surface nuclear magnetic resonance in the Vadose Zone, *Vadose Zone J.,* **13**(11), 1–9.

Dlugosch, R., Günther, T., Müller-Petke, M. & Yaramanci, U., 2013. Improved prediction of hydraulic conductivity for coarse-grained, unconsolidated material from nuclear magnetic resonance, *Geophysics,* **78**(4), EN55–EN64.

Dlugosch, R., Günther, T., Müller-Petke, M. & Yaramanci, U., 2014. Two-dimensional distribution of relaxation time and water content from surface nuclear magnetic resonance, *Near Surf. Geophys.,* **12,** 231–241.

Grombacher, D., 2018. Numerically optimized modulations for adiabatic pulses in surface nuclear magnetic resonance, *Geophysics,* **83**(2), JM1–JM14.

Grombacher, D., Behroozmand, A.A. & Auken, E., 2017. Accounting for relaxation during pulse effects for long pulses and fast relaxation times in surface nuclear magnetic resonance, *Geophysics,* **82**(6), JM23–JM36.

Grunewald, E., Grombacher, D. & Walsh, D., 2016. Adiabatic pulses enhance surface nuclear magnetic resonance measurement and survey speed for groundwater investigations, *Geophysics,* **81**(4), WB85–WB96.

Günther, T. & Müller-Petke, M., 2012. Hydraulic properties at the North Sea island of Borkum derived from joint inversion of magnetic resonance and electrical resistivity soundings, *Hydrol. Earth Syst. Sci.,* **16**, 3279–3291.

Hertrich, M., 2008. Imaging of groundwater with nuclear magnetic resonance, *Prog. Nucl. Magnet. Reson. Spectrosc.,* **53**(4), 227–248.

Hertrich, M., Braun, M., Günther, T., Green, A.G. & Yaramanci, U., 2007. Surface nuclear magnetic resonance tomography, *IEEE Trans. Geosci. Remote Sens.,* **45**(11), 3752–3759.

Jiang, C., Liu, J., Tian, B., Sun, S., Lin, J & Müller-Petke, M., 2016. 3D block QT inversion of surface nuclear magnetic resonance data, *Geophysics,* **81**(5), WC19–WC32.

Jiang, C., Igel, J., Dlugosch, R., Günther, T. & Müller-Petke, M., 2017. Aquifer imaging using 2D magnetic resonace tomography with structural constraints from GPR, in *Proceedings of the 23rd European Meeting of Environmental and Engineering Geophysics,* pp. 1–5.

Jiang, C., Müller-Petke, M., Wang, Q. & Igel, J., 2018. Two-dimensional QT inversion of complex magnetic resonance tomography data, *Geophysics,* **83**(6), JM65–JM75.

Larsen, J.J., Dalgaard, E. & Auken, E., 2014. Noise cancelling of MRS signals combining model-based removal of powerline harmonics and multi-channel Wiener filtering, *Geophys. J. Int.,* **196**(2), 828–836.

Legchenko, A. & Valla, P., 2002. A review of the basic principles for proton magnetic resonance sounding measurements, *J. appl. Geophys.,* **50**(1–2), 3–19.

Legchenko, A., Baltassat, J.M., Bobachev, A., Martin, C., Robain, H. & Vouillamoz, J.-M., 2004. Magnetic resonance sounding applied to aquifer characterization, *Ground Water,* **42**(3), 363–373.

Legchenko, A., Descloitres, M., Vincent, C., Guyard, H., Garambois, H., Chalikakis, K. & Ezersky, M., 2011. Three-dimensional magnetic resonance imaging for groundwater, *New J. Phys.,* **13**(025022), 1–17.

Levitt, M.H., 2002. *Spin Dynamics - Basics of Nuclear Magnetic Resonance,* John Wiley & Sons, LTD.

Lin, T., Yang, Y., Teng, F. & Müller-Petke, M., 2018a. Enabling surface nuclear magnetic resonance at high-noise environments using a pre-polarization pulse, *Geophys. J. Int.,* **212**(2), 1463–1467.

Lin, T., Zhou, K., He, C., Wang, P., Zhang, Y. & Xu, Y., 2018b. Analysis and design of the transmitting mode on the pre-polarization surface nuclear magnetic resonance system, *Rev. Scient. Instrum.,* **89**(12), 125102.

Lin, T., Yang, Y., Yang, Y., Wan, L. & Teng, F., 2019. Exploiting Adiabatic pulses with prepolarization in detection of underground nuclear magnetic resonant signals, *IEEE Transactions on Geoscience and Remote Sensing,* pp. 1–10.

Melton, B.F. & Pollak, V.L., 1971. Instrumentation for the Earth's field NMR technique, *Rev. Sci. Instrum.,* **42**(6), 769–773.

Melton, B.F. & Pollak, V.L., 2002. Condition for adiabatic passage in the earths-field NMR technique, *J. Magn. Reson.,* **158**(1–2), 15–22.

Melton, B.F., Pollak, V.L., Mayes, T.W. & Willis, B.L., 1995. Condition for sudden passage in the Earths-field NMR technique, *J. Magn. Reson., A,* **117**(2), 164–170.

Mohnke, O. & Yaramanci, U., 2008. Pore size distributions and hydraulic conductivities of rocks derived from Magnetic Resonance Sounding relaxation data using multi-exponential decay time inversion, *J. appl. Geophys.,* **66**(3-4), 73–81.

Müller-Petke, M. & Costabel, S., 2014. Comparison and optimal parameter setting of reference-based harmonic noise cancellation in time and frequency domain for surface-NMR, *Near Surf. Geophys.,* **12**, 199–210.

Müller-Petke, M. & Yaramanci, U., 2010. QT inversion—comprehensive use of the complete surface NMR data set, *Geophysics,* **75**(4), WA199–WA209.

Müller-Petke, M., Braun, M., Hertrich, M., Costabel, S. & Walbrecker, J., 2016. MRSmatlab—a software tool for processing, modeling, and inversion of magnetic resonance sounding data, *Geophysics,* **81**(4), WB9–WB21.

Packard, M. & Varian, R., 1954. Free nuclear induction in Earth's magnetic field, *Phys. Rev.,* **93**(4), 941.

Planinšič, G., Stepišink, J. & Kos, M., 1994. Relaxation-time measurement and imaging in the Earth's magnetic-field, *J. Magn. Reson., A,* **110**(2), 170–174.

Powles, J.G., 1958. The adiabatic fast passage experiment in magnetic resonance, *Proc. Phys. Soc.,* **71**(3), 497–500.

Seevers, D.O., 1966. A nuclear magnetic method for determining the permeability of sandstones, in *Proceedings of the SPWLA 7th Annual Logging Symposium,* Vol. **Paper L,** p. 14, Tulsa, Oklahoma.

Shampine, L.F. & Reichelt, M.W., 1997. The MATLAB ODE suite, *SIAM J. Scient. Comput.,* **18**(1), 1–22.

Skibbe, N., Güther, T. & Müller-Petke, M., 2018. Structurally coupled co-operative inversion of magnetic resonance with resistivity soundings, *Geophysics,* **83**(6), JM51–JM63.

Tannùs, A. & Garwood, M., 1997. Adiabatic pulses, *NMR Biomed.,* **10**(8), 423–434.

Uğurbil, K., Garwood, M. & Rath, A.R., 1988. Optimization of modulation functions to improve insensitivity of adiabatic pulses to variations in B_1 magnitude, *J. Magnet. Reson.,* **80**(3), 448–469.

van Zijl, P. C.M., Hwang, T.-L., O'Neil Johnson, M. & Garwood, M., 1996. Optimized excitation and automation for high-resolution NMR using B_1-insensitive rotation pulses, *J. Am. Chem. Soc.,* **118**(23), 5510–5511.

Vouillamoz, J.M., Chatenoux, B., Mathieu, F., Baltassat, J.M. & Legchenko, A., 2007. Efficiency of joint use of MRS and VES to characterize coastal aquifer in Myanmar, *J. appl. Geophys.,* **61**(2), 142–154.

Vouillamoz, J.M., Legchenko, A. & Nandagiri, L., 2011. Characterizing aquifers when using magnetic resonance sounding in a heterogeneous geomagnetic field, *Near Surf. Geophys.,* **9**(2), 135–144.

Weichman, P.B., Lavely, E.M. & Ritzwoller, M.H., 2000. Theory of surface nuclear magnetic resonance with applications to geophysical imaging problems, *Phys. Rev. E,* **62**(1), 1290–1312.

APPENDIX: VERIFICATION OF SPIN DYNAMICS MODELLING

To validate our implementation of eq. (6), we use two published examples that study the effect of different switch-off characteristics on pre-polarization effectiveness. The first is from Melton *et al.* (1995), where the authors use linear switch-off ramps with varying switch-off rates, to find a criteria for the so-called sudden passage (the opposite of adiabatic passage). The second example is from Conradi *et al.* (2017), where the authors use switch-off ramps that consist of an early linear and a late exponential part. In their work, the authors show how the cross-over field strength B^* between these two regimes influences the adiabatic quality of the switch-off, depending on the initial orientation of $\mathbf{B}_0$ and $\mathbf{B}_p$.

A schematic representation of the geometry involved in these two studies and this work is shown in Fig. A1(a). By convention, the primary field $\mathbf{B}_0$ is collinear with the *z*-axis. The angle θ describes the orientation between the Earth's magnetic field $\mathbf{B}_0$ and the $\mathbf{B}_p$-field prior to switch-off. The angle α is the angle between $\mathbf{B}_0$ and $\mathbf{B} = \mathbf{B}_0 + \mathbf{B}_p$ that varies during switch-off as $\mathbf{B}$ moves from its initial orientation towards $\mathbf{B}_0$. The polar and azimuthal angles ϕ_p and ϕ_a describe the final orientation of $\mathbf{M}_p$ with regard to $\mathbf{B}_p$.

In the first example, the initial angle is fixed at $\theta = 90°$ and the amplitude of the PP-field is $B_p = 100 \cdot B_0$ with $B_0 = 50\ \mu$T. Fig. A1(b) shows the angles ϕ_p and ϕ_a as a function of the dimensionless switch-off rate $100/\omega_L/\tau_r$. Melton *et al.* (1995) found that the larger the switch-off rate is (shorter ramp time), the larger is the deviation
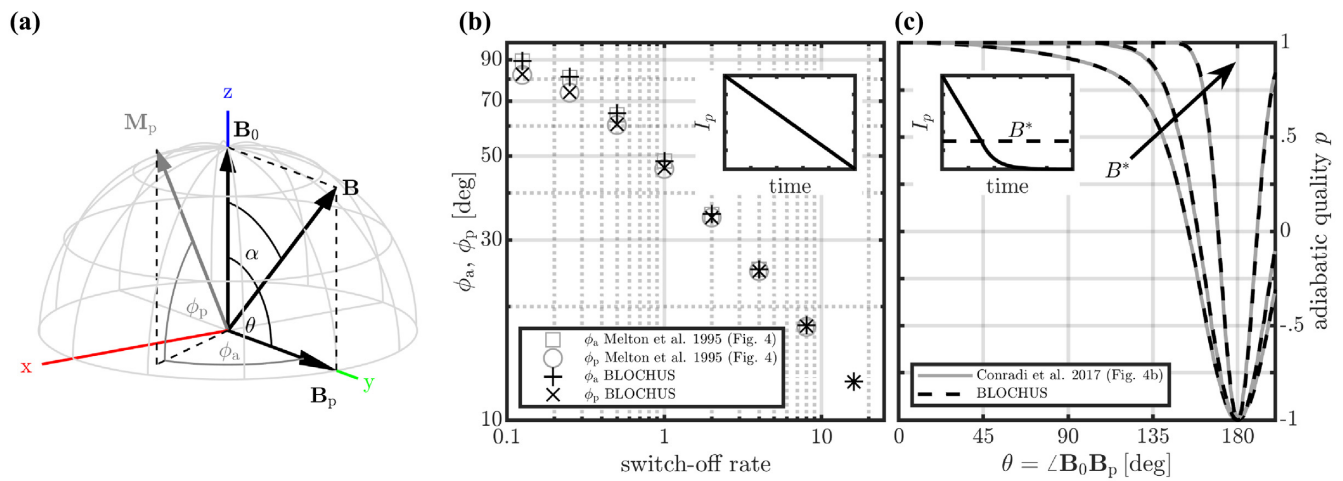
(a)

(b)

(c)

Figure A1. (a) Sketch of the geometrical relations used in this work; (b) comparison of our implementation (black symbols) to Melton *et al.* (1995) (grey symbols), azimuthal and polar angles ϕ_a and ϕ_p as a function of switch-off rate (see text); (c) comparison of our implementation (black dashed lines) to Conradi *et al.* (2017) (grey lines), adiabatic quality p as a function of initial angle θ for three different cross-over field strengths B^*.

of the final orientation of $\mathbf{M}_p$ with regard to $\mathbf{B}_0$, and hence, the switch-off is no longer adiabatic. The grey symbols in Fig. A1(b) refer to the results of Melton *et al.* (1995) and the black symbols are modelled with BLOCHUS. We see an excellent agreement over the whole range of switch-off rates.

In the second example the $\mathbf{B}_p$-field amplitude is $B_p = 50 \cdot B_0$ with $B_0 = 50\ \mu\text{T}$ and the switch-off ramp time is fixed to $\tau_r = 20\text{ms}$. We plot the adiabatic quality p as a function of initial angle $\theta \in [0°, 200°]$ (Fig. A1c). The grey curves in Fig. A1(c) refer to the results

of Conradi *et al.* (2017) for different cross-over field strengths B^*. They show that the larger the cross-over field strength is, the better is the adiabatic quality over a wider range of initial angles θ. For this particular set of parameters, this means that the earlier the switch to the exponential regime happens, the more adiabatic is the switch-off. Again, our results (black dashed curves) show an excellent agreement with the published data. For the details of the two studies, we refer the reader to Melton *et al.* (1995) and Conradi *et al.* (2017).